

Fiberfox: An Extensible System for Generating Realistic White Matter Software Phantoms

Peter F. Neher, Frederik B. Laun, Bram Stieltjes, and Klaus H. Maier-Hein

Abstract We present an open-source system, Fiberfox, for generating synthetic diffusion-weighted datasets. Fiberfox enables (1) definition of artificial white matter fibers, (2) signal generation from those fibers using multi-compartment modeling, and (3) simulation of magnetic resonance artifacts including Gibbs ringing, $N/2$ ghosting and susceptibility distortions. With a comparative hardware phantom study we show that the synthetic datasets closely resemble real acquisitions. To demonstrate the relevance of Fiberfox for current research questions, we reveal the adverse effects of anisotropic voxels on the outcome of 11 different fiber tractography algorithms. Fiberfox is openly available and may find application in the validation and further development of diffusion-weighted image processing techniques such as super-resolution, denoising, tractography, diffusion modeling or artifact correction.

P.F. Neher (✉)

Medical and Biological Informatics, German Cancer Research Center (DKFZ), Heidelberg, Germany

e-mail: p.neher@dkfz.de

F.B. Laun

Medical Physics in Radiology & Quantitative Image-based Disease Characterization, German Cancer Research Center (DKFZ), Heidelberg, Germany

e-mail: f.laun@dkfz.de

B. Stieltjes

Quantitative Image-based Disease Characterization, German Cancer Research Center (DKFZ), Heidelberg, Germany

e-mail: b.stieltjes@dkfz.de

K.H. Maier-Hein

Medical and Biological Informatics & Quantitative Image-based Disease Characterization, German Cancer Research Center (DKFZ), Heidelberg, Germany

e-mail: k.maier-hein@dkfz.de

1 Introduction

Over the last few years an abundance of new techniques for processing of diffusion-weighted images have been introduced. Two main objectives in this field are the correct depiction of macroscopic connectivity and the quantification of microstructural features of brain tissue. However, the organization of human brain tissue is highly complex which renders the proper definition of in-vivo reference datasets challenging. Hence validation has become its own field of research [6] and has led to the development of numerous phantom-based approaches that aim for reliable reference data on the one hand and realism of the experiments on the other. Due to their unique property of providing the reference together with the data itself synthetic datasets and software phantoms are widely used [1, 7]. However, many existing approaches are restricted to generating diffusion signals of single voxels (Camino,¹ MCF²), which makes them unsuitable for methods that require a reference to neighboring voxels or structures, such as fiber tractography, connectomics and tract-based spatial statistics (TBSS). Furthermore, voxel-wise approaches are not capable of simulating many of the artifacts occurring in MRI acquisitions, since a complete image is required for such simulations. Other methods simulate whole image volumes ([3], Tend Helix³), but provide limited options for the interactive definition of complex fiber geometries or advanced signal modeling approaches. Effects like thermal noise, Gibbs ringing, relaxation-induced blurring or image distortions due to magnetic inhomogeneities, are not represented in currently available software phantoms but play a significant role in the final data analysis.

We present an open-source system, Fiberfox, that enables complex voxel-wise diffusion modeling in combination with the synthesis of whole images of arbitrary fiber configurations. Fiberfox is implemented in a modular fashion that facilitates an easy exchange or extension of different signal and artifact models. In this article, we demonstrate the capabilities of Fiberfox by generating diffusion-weighted datasets of numerous fiber configurations with different levels of structural complexity and examine the degree of realism reached by the synthetic datasets in a hardware phantom study. As an exemplary application, we quantify the impact of anisotropic voxels on 11 commonly used fiber tractography algorithms. To assure reproducibility, comparability, and extensibility of research on the basis of Fiberfox, and to maximize the benefit to the community [5], Fiberfox is published open-source and is integrated into the 2013.06 release of MITK Diffusion [4] (www.nitrc.org/projects/mitk-diffusion/).

¹<http://cmic.cs.ucl.ac.uk/camino/>

²<http://www.nitrc.org/projects/mcftool/>

³<http://teem.sourceforge.net/>

2 Materials and Methods

The phantom generation process involves three steps: (1) the interactive definition of the fiber geometry, (2) the generation of synthetic diffusion-weighted datasets from these fibers and (3) the simulation of artifacts in the data.

2.1 Fiber Definition

Fiberfox enables the user to define fiber strands of any desired shape (e.g. straight, bent, crossing, kissing, twisting and fanning configurations), by placing markers in 3D space. The fiducials are realized as 2D ellipses which can be drawn with only a few mouse clicks. We chose an elliptical shape for the fiducials because it facilitates an easy placement and adjustment but is flexible enough to approximate a wide range of fiber profile shapes. To generate fibers following the path defined by the fiducials, a user defined number of seed points for the fibers are automatically distributed in the first ellipse following the selected distribution (e.g. Gaussian). The seed points thus placed are then propagated to the succeeding fiducials to serve as waypoints for the interpolation with Kochanek-Bartels splines. The generated fiber bundles can be copied and spatially transformed to provide well-defined situations, e.g. two strands with a crossing angle of exactly 45° .

2.2 Signal Generation

To generate an artificial signal S from the input fibers we follow the concepts recently presented by Panagiotaki et al. in a review and taxonomy of different compartment models [9]: a flexible model combining multiple compartments $S_{v,i}$ is used to simulate the anisotropic diffusion inside and between axons, isotropic diffusion outside of the axons and the restricted diffusion in other cell types weighted according to their respective volume fraction $f_{v,i}$ in voxel v . The signal of N compartments simulated for v in gradient direction g is calculated by:

$$S_v(g) = \sum_i^N f_{v,i} S_{v,i}(g) \quad (1)$$

Currently our framework includes various combinations of the *stick*, *tensor*, *zeppelin*, *ball*, *dot* and *astrosticks* diffusion models [9]. In our experiments we used a *ball-zeppelin* model simulating the isotropic diffusion of free water (S_1) and the anisotropic diffusion in the fiber tissue (S_2):

$$S_v(g) = f_{v,1}e^{-bD_1} + (1 - f_{v,1}) \sum_{p \in P} \int_p e^{-bg^T D_{2,t(x)}g} dx \quad (2)$$

where D_1 is the scalar diffusivity in the free water compartment, P is the set of all fiber paths p present inside v , b is the used diffusion weighting in s/mm^2 , $t(x)$ is the direction of the fiber tangent at position x along fiber path p and $D_{2,t(x)}$ is the cylindrically symmetric second order tensor defining the anisotropic diffusivity in the fiber compartment with the largest eigenvector pointing into the direction of $t(x)$.

2.3 Artifact Simulation

Single-shot echo planar imaging (EPI) sequences, as commonly used in diffusion-weighted imaging, are prone to a wide range of imaging artifacts. Our framework allows for the simulation of several relevant artifacts [2] each of which is illustrated on an exemplary structure:

- Thermal noise (Fig. 1a) is simulated using a Rician distribution.
- Relaxation induced blurring (Fig. 1b): Depending on the two relaxation constants $T2$ and $T2'$ as well as the echo time TE , the exponential decay of the signal during the application of the readout gradient is modeled.
- Gibbs ringing (Fig. 1c): The limited image matrix and consequent low-pass filtering of the frequency spectrum causes ringing artifacts in the image. This effect is simulated by cropping a high resolution version of the k-space image \hat{S} to the desired image size.
- Magnetic field inhomogeneities (Fig. 1d, f): Distortions due to imperfections of the constant magnetic field are modeled by adding a time and location dependent phase $\phi(t, r)$ to the signal. The k-space signal can thus be calculated by

$$\hat{S}(k) = \int \rho(r) e^{i(kr + \phi(t-TE, r))} dr$$

where k is the spatial frequency and $\rho(r)$ is the spin density at location r . A user defined frequency map specifying the magnetic field distortions across the image volume is used as input for the algorithm.

- $N/2$ ghosting (Fig. 1d, f): This effect is caused by a zigzag offset between the even and odd k-space lines in phase direction. We simulate this artifact by adding a user defined delay time to the frequency encoding gradients which causes such an offset due to the alternating signs of the readout gradients.

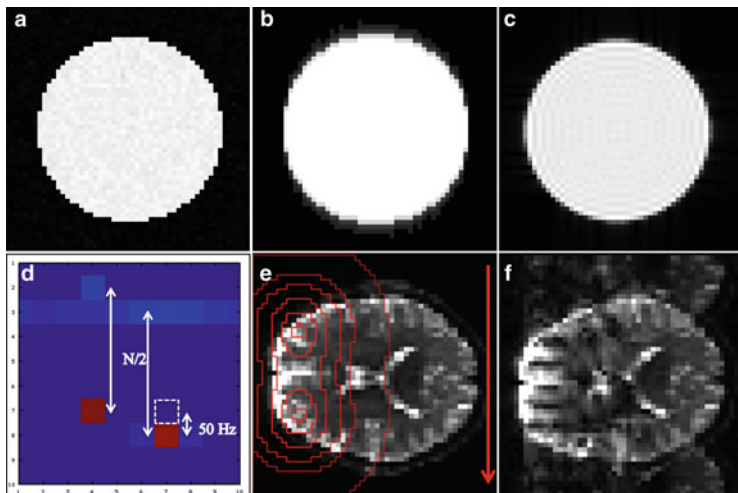


Fig. 1 Artifacts included in Fiberfox: Illustration of Rician noise (a), blurring (b) and Gibbs ringing (c) artifacts added to the simulated acquisition of a circular object with a radius of 20 voxels. (d) Illustrates the susceptibility distortion and ghosting artifact on a simple example. A magnetic field inhomogeneity of 50 Hz at pixel (7,7) shifts the *red pixel* exactly one pixel down in the vertical (phase) direction. The $N/2$ ghosts of the two points are clearly visible in the upper part of (d). (f) Shows the distortion and ghosting effect on an axial slice of an in-vivo acquisition (e). The frequency map (depicted with *red isolines* in the undistorted image (e)) was generated using two Gaussian distributions in the region of the forehead with values ranging from 0 Hz to about 100 Hz. In the upper and lower part of (f) one can clearly observe the $N/2$ ghosting artifacts introduced by a slight offset of the readout gradients of about $8 \cdot 10^{-4}$ ms while the frontal region of the brain is deformed in phase direction (*red arrow*)

2.4 Simulations and Experiments

To demonstrate the capabilities of Fiberfox we generated several relevant fiber configurations and the corresponding phantom images. The authenticity of the synthetic image generation was evaluated by comparing measured data obtained from two hardware phantoms to the artificial signal of two fiber sets with corresponding configurations. We acquired diffusion-weighted images from one hardware phantom with a single fiber strand and one crossing phantom with two fiber strands intersecting in a 90° angle. The phantoms consist of polyester fibers wound around a plastic spindle and enclosing a sodium chloride solution [8]. Images of the single strand phantom were acquired on a 1.5 T Siemens Magnetom Avanto scanner employing a single shot EPI with a resolution of $1.6 \times 1.6 \times 1 \text{ mm}^3$, 6 gradient directions with a diffusion weighting of $b = 500 \text{ s/mm}^2$ and 32 averages. The image of the crossing phantom was obtained using a single shot EPI on a 3 T Siemens Magnetom Trio scanner with a voxel spacing of $2.5 \times 2.5 \times 7 \text{ mm}^3$, 252 gradient directions and b-values of $1,000 \text{ s/mm}^2$. We used the same parameters to generate the artificial images as employed for the original acquisitions of the phantoms.

Furthermore, we used Fiberfox to investigate the impact of anisotropic voxels on the outcome of 11 commonly used fiber tractography algorithms ranging from simple tensor streamlining over probabilistic methods and more sophisticated modeling techniques to global approaches. To this end, a fiber configuration similar to the corticospinal tract (CST) was designed using Fiberfox. Three datasets were generated, simulating a b-value of $1,000 \text{ s/mm}^2$, 30 gradient directions and a noise variance of 25, which are realistic parameters for a clinical acquisition. The first dataset was generated with an isotropic resolution of 1 mm. The second and third image were generated with a decreased resolution along the z-axis of 2 and 4 mm respectively. Vice versa, the anisotropic images were upsampled to an isotropic resolution, thus allowing the comparison of tractography on the natively isotropic image vs. tractography on the merely upsampled isotropic datasets. We evaluated the amount of fibers connecting the seed region in the inferior part with a ROI placed in the lateral part of the phantom. The location of the lateral ROI (Fig. 4a) was chosen since it corresponds to the part of the motor cortex that is the most challenging to be reached by tracking methods trying to reconstruct the CST as it was shown during the DTI Tractography Challenges MICCAI 2011/2012 [10].

3 Results

Figure 2 illustrates examples of twisting, fanning, highly curved and kissing bundles as well as of the corresponding tensor images. The tensor reconstructions of the synthetic images clearly reflect the structure of the corresponding fiber set and realistic partial volume effects, e.g. at fiber bundle margins, can be observed.

Figure 3 shows the comparison between the real images obtained from the hardware phantoms (a, c) and the corresponding synthetic images generated with Fiberfox (b, d). Figure 3 shows the baseline volume of the real (a) and the synthetic (b) single strand phantom acquisition. Figure 3c, d show the generalized fractional anisotropy (GFA) maps derived from the diffusion-weighted datasets superimposed by the maximum normalized glyph representation of the corresponding constant solid angle Q-ball reconstruction.

Figure 4a shows the fiber phantom used to analyze the effects of anisotropic voxels on the outcome of five widely used tractography algorithms as described in Sect. 2.4. Six out of 11 algorithms failed to reach the target ROI in all datasets, including the natively isotropic dataset. Figure 4b shows the results of the remaining five algorithms. The diagram depicts the percentage of fibers reaching the target ROI when tracking on the anisotropic and upsampled datasets compared to the natively isotropic dataset. The results demonstrate the substantial influence of voxel geometry on the tractography outcome. Moreover it can be seen that the actual loss (between 20 and 100 % in the $1 \times 1 \times 4 \text{ mm}^3$ case) is highly algorithm dependent and only for some algorithms partially reversible by resampling the datasets.

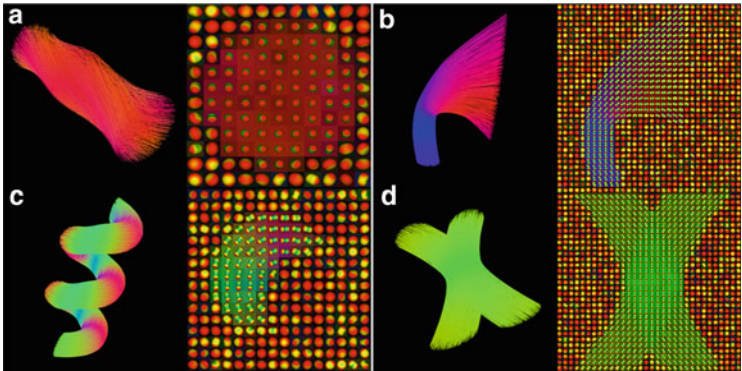


Fig. 2 Fiber configurations generated with Fiberfox: Examples of twisting (a), fanning (b), highly curved (c) and kissing (d) fibers, colored according to the tangent direction, as well as of the corresponding tensor images generated with Fiberfox. The tensor images are represented as color maps indicating the direction of largest diffusion superimposed by the maximum normalized glyphs of the radially projected diffusion tensors

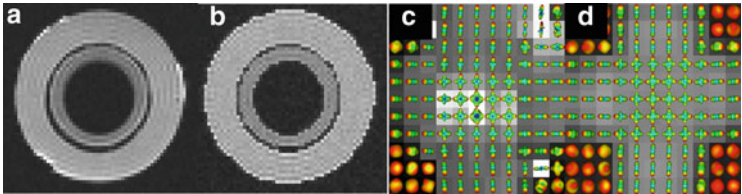


Fig. 3 Comparison of Fiberfox data and hardware phantom data: (a) depicts a real acquisition of the single strand hardware phantom. The corresponding synthetic image generated with Fiberfox including Gibbs ringing, blurring and added Rician noise is shown in (b). The outer ring is formed by the agarose gel surrounding the phantom spindle and the inner ring consists of the coiled polyester fibers. (c) and (d) show the GFA images obtained from the original and the simulated datasets depicting a 90° crossing fiber configuration superimposed by the glyph representation of the corresponding Q-ball reconstruction

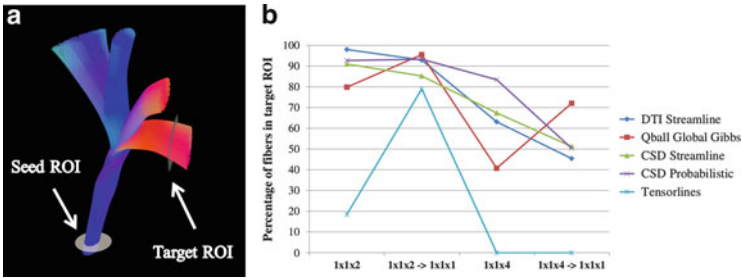


Fig. 4 Evaluation of tractography on anisotropic voxels: (a) fiber phantom mimicking the corticospinal tract, generated with Fiberfox. (b) Percentage of fibers in the target ROI relative to the tractography at natively isotropic resolution

4 Discussion and Conclusion

We presented Fiberfox, an open-source system that enables the interactive generation of white matter fiber phantoms and demonstrated its potential in several experiments.

Our experimental results showed that anisotropic image resolutions clearly hamper the already challenging tractography of laterally diverging fiber strands. This supports the observations during the recent MICCAI DTI Tractography Challenges where many algorithms failed in reconstructing the lateral fibers of the CST. Our findings suggest that the usage of acquisition protocols with anisotropic image resolution, which is especially common in clinical settings, is in general not recommendable for fiber tractography.

Possible further applications for Fiberfox include the quantitative evaluation of super-resolution approaches, denoising, tractography, diffusion modeling, artifact correction, connectomics or methods like voxel-based morphometry and TBSS. It could also support and complement the evaluation and data generation strategies currently pursued at events such as the DTI Tractography Challenge (MICCAI) or the HARDI Reconstruction Challenge (ISBI).

Further extensions of Fiberfox could include the implementation of effects like non-constant sensitivity profiles of the receiver coils, frequency dependent chemical shifts, motion artifacts and non-Rician thermal noise [2]. Additionally, alternative models such as the kurtosis tensor model or model-free approaches such as Monte Carlo simulations of diffusion could be integrated. While the current implementation already provides a rich set of signal and artifact models suitable for many tasks [9], the modular framework of Fiberfox supports many of such extensions in a plug-and-play fashion. We believe that Fiberfox is a valuable addition to the currently available repertoire of open-source software phantom generation tools. Support for commonly used data formats ensures usability and raises its benefit to the community. By making it publicly available we hope that Fiberfox can contribute to driving innovation in the field of diffusion-weighted image processing.

References

1. Basser, P.J., Pajevic, S., Pierpaoli, C., Duda, J., Aldroubi, A.: In vivo fiber tractography using dt-mri data. *Magn. Reson. Med.* **44**, 625–632 (2000)
2. Bihan, D.L., Poupon, C., Amadon, A., Lethimonnier, F.: Artifacts and pitfalls in diffusion MRI. *Magn. Reson. Imaging* **24**, 478–488 (2006)
3. Close, T.G., Tournier, J.D., Calamante, F., Johnston, L.A., Mareels, I., Connelly, A.: A software tool to generate simulated white matter structures for the assessment of fibre-tracking algorithms. *Neuroimage* **47**, 1288–1300 (2009)
4. Fritzsche, K., Neher, P., Reicht, I., van Bruggen, T., Goch, C., Reisert, M., Nolden, M., Zelzer, S., Meinzer, H.P., Stieltjes, B.: Mitk diffusion imaging. *Method Inform. Med.* **51**(5), 441–448 (2012)

5. Ince, D., Hatton, L., Graham-Cumming, J.: The case for open computer programs. *Nature* **482**, 485–488 (2012)
6. Jannin, P., Krupinski, E., Warfield, S.: Validation in medical image processing. *IEEE Trans. Med. Imaging* **25**(11), 1405–1409 (2006)
7. Jones, D.K., Basser, P.J.: Squashing peanuts and smashing pumpkins: how noise distorts diffusion-weighted MR data. *Magn. Reson. Med.* **52**, 979–993 (2004)
8. Moussavi-Biugui, A., Stieltjes, B., Fritzsche, K., Semmler, W., Laun, F.B.: Novel spherical phantoms for Q-ball imaging under in vivo conditions. *Magn. Reson. Med.* **65**, 190–194 (2011)
9. Panagiotaki, E., Schneider, T., Siow, B., Hall, M.G., Lythgoe, M.F., Alexander, D.C.: Compartment models of the diffusion MR signal in brain white matter: a taxonomy and comparison. *Neuroimage* **59**, 2241–2254 (2012)
10. Pujol, S., Kikinis, R., Golby, A., Gerig, G., Styner, M., Wells, W., Westin, C., Gouttard, S.: DTI tractography for neurosurgical planning: a grand challenge. In: MICCAI, Toronto (2011)

Computational Diffusion MRI and Brain Connectivity
MICCAI Workshops, Nagoya, Japan, September 22nd,
2013

Schultz, Th.; Nedjati-Gilani, G.; Venkataraman, A.;
O'Donnell, L.; Panagiotaki, E. (Eds.)

2014, XIV, 255 p. 78 illus., 67 illus. in color., Hardcover
ISBN: 978-3-319-02474-5